Study on fracture behaviors of concrete using electronic speckle pattern interferometry and finite element method

Helen Hongniao Chen[1], Ray Kai Leung Su[1]

Summary

In this study, Electronic Speckle Pattern Interferometry (ESPI) technique was used to measure the surface displacement and strain fields around cracks in concrete beams. ESPI has high accuracy and can determine full-field deformations of concrete. However, tiny rigid-body movements of beam specimens can spoil the ESPI measurement and cause virtual deformations and false strains. Based on the theory of geometrical optics, this paper proposes a method to eliminate the false strains caused by rigid-body motion. The correction procedure was validated experimentally. Furthermore, the crack evolution in a pre-notched beam is presented. The critical minimum crack width of a microcrack is found to be about 0.1μm and the minimum crack width of an open crack is about 2 μm. Finally, a finite element analysis of a notched beam was conducted. The numerical and experimental results reveal that the critical crack tip opening of a notched beam is around 30-35 μm.

Keywords: Fracture behaviors; Concrete; ESPI; Rigid-body motion; ATENA software

Introduction

Since the ultimate load capacity of concrete structures depends on the evolution of cracks, it is important to study the fracture behavior of concrete. Due to the mechanisms such as micro-cracking, crack deflection, aggregate bridging, and crack branching, the fracture behavior of concrete with internal cracks is very complicated. In order to study the fracture behavior of concrete with cracks, the concept of a fracture process zone ahead the crack tip was proposed and the characterization of fracture process zones has become a challenge in the past decades.

Due to the fact that micro-cracks in concrete are invisible, the study of fracture mechanisms, followed the advances in measurement technology, has recently come through a series of developments: surface wave transmission, microscope measuring, strain gauge techniques, dye penetrants, ultrasonic measuring, acoustic emission, interferometry techniques and so on. Strain gauge is the most common measuring instrument. However, it can only provide an average value over a certain gauge length rather than the local deformation at all points on the measuring surface. The local deformations, particularly near the crack tip, are significant to

---

[1]Department of Civil Engineering, the University of Hong Kong, Hong Kong

the study of fracture mechanics. Furthermore, the actual crack path in the specimen without a pre-notch is usually not known prior to the test, hence it is hard to attach strain gauges on the region of interests. ESPI can overcome the aforementioned limitations and enable a full-field surface deformation measurement. It is an effective tool for the investigation of fracture process zones in concrete.

With its high precision, ESPI has been applied to measure the deformation of many materials. Celdolin et al. (1987) conducted interferometric measurement on concrete specimens and obtained local stress-strain and stress-separation relations near a notch. Castro-Montero et al. (1990) carried out experiments on a center-notched mortar plate and used a holographic setup to detect the crack opening and strain fields along the crack trajectories. Jia and Shah (1995) used a two-dimensional ESPI system to monitor the fracture process of concrete. They analyzed the displacement and strain fields, and provided some quantitative results of cracks. Cao et al. (2007) used ESPI to study the bond-slip relationships of FRP-concrete. Restivo and Cloud (2008) carried out measurement on a polymethyl-methacrylate beam and disc specimen, and demonstrated the validity of using an ESPI system for strain analysis. Haggerty et al. (2009) used ESPI to observe the fracture deformation of rock. Although, the aforementioned studies have shown that ESPI technique is able to measure surface deformations of different materials, only a few studies were conducted for measuring the fracture process of concrete.

However, tiny rigid-body motion ($<10\mu$m) can affect the accuracy of the measurement. ESPI regards rigid-body movements as deformations and provides false information in the measurement results. Since tiny rigid-body movements of the specimen cannot be avoided in a loading test, a correction process is necessary to eliminate the influence of rigid-body motion.

In this study, a correction method is proposed to eliminate the influence of rigid-body motion in ESPI deformation measurements. The corrected crack opening displacements in concrete are determined and presented. In addition, a finite element analysis using the computer package, ATENA (2000), was conducted to verify the validity of different softening laws by comparing the numerical results with the experimental results.

Specimen and Experimental Setup

Specimens and Material Proportions

Unnotched and notched concrete beams were cast for four-point and three-point bending tests respectively. The specimen size (span × depth × thickness) is 600 × 150 × 70 mm. The initial notch length and width of the notched beam are 60 mm and 3 mm respectively. The specimen dimension was designed according to the preference proposed by RILEM (1990) on Fracture Mechanics. The concrete mix

proportions are tabulated in Tab. 1. The coarse aggregates are produced from crushed granite.

Table 1: Material proportions by weight

Material	Unnotched Beam	Notched Beam
Water (kg/m^3)	200	173
Cement (kg/m^3)	279	482
Fine Aggregate (kg/m^3)	1025	867
Coarse Aggregate (kg/m^3)	838	866
Max. Aggregate size (mm)	5	10
Cube Strength (MPa)	35.2	79.4
Elastic Modulus (MPa)	23586	32317

Experimental Setup

Using an MTS bending fixture, four-point and three-point bending tests were carried out. The experimental setups are shown in Fig. 1.
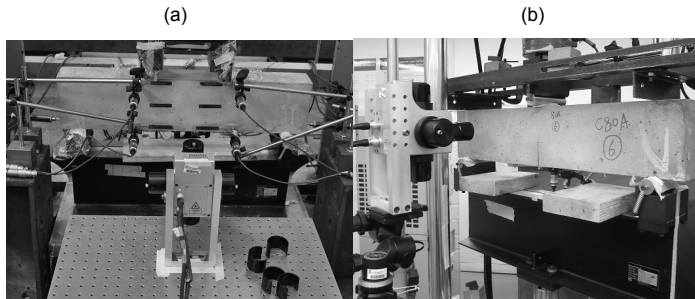

Figure 1: Experimental setup of: (a) four-point bending test and (b) three-point bending test

In the four-point bending test, the deformation of concrete in pure bending zone was measured by both ESPI and strain gauges. By comparing the corrected ESPI results and strain gauge readings, the accuracy of the correction procedure was verified. Linear variable differential transformers (LVDTs) were used to measure the rigid-body motion of the measuring surface. The locations of strain gauges and LVDTs are shown in Fig. 1(a).

Since the crack path of the main crack in the four-point bending test has not been known prior to the test, three-point bending tests on notched beam were carried out to investigate the crack evolution. As expected, for a notched beam, the main crack initiated from the tip of the pre-notch.

Theoretical Backgrounds

Principles of ESPI System

The principle of ESPI is based on the interference of two coherent laser beams (a reference beam and an observation beam). In the measurement, the two beams are reflected and scattered by the rough measuring surface. The reflected beams are overlaid and produce a speckle pattern, which is recorded by a Charge Coupled Device (CCD) camera. By subtracting two speckle patterns at different states, before deformation and after deformation, interference fringes can be obtained. Using the four-step phase shifting method, the phase difference between two states, also known as wrapping phase map, can be calculated. Applying the phase-shift process, the unwrapping phase map including the displacement field can be obtained. By calculus, the strain field of the measuring surface is evaluated. ISTRA software is used to generate displacement and strain contour maps.

Estimation of the Influence of Rigid-Body Motion

Due to the intrinsic limitation of ESPI, rigid-body movements of the measuring surface can produce some false strains in the geometric optics calculations. The measuring surface has six types of rigid-body movements, which correspond to three translational displacements (S_x, S_y and S_z) and three rotational displacements (R_x, R_y and R_z) as shown in Fig. 2:
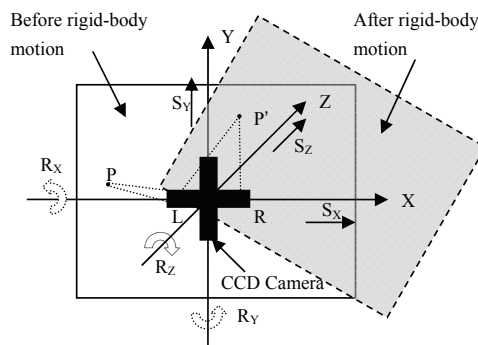

Figure 2: Rigid-body motion of the measuring surface

Assuming the camera center is at the origin (0, 0, 0) of the Cartesian coordinates and the measuring surface is located at the plane $z=d$, the observation beam and reference beam come out from the left lens L ($-l_x$, 0, 0) and the right lens R (l_x, 0, 0) respectively. Without loss of generosity, considering a point $P=(x,y,d)$ on the measuring surface, after rigid-body motion, point P moves to $P'=(x+d_x, y+d_y, z+d_z)$, where d_x, d_y, d_z are the global displacements of point P due to the rigid-body motion.

In this calculation, the measuring surface is assumed to be un-deformed. Be-

fore the rigid-body motion, the paths of the observation beam and reference beam in Fig. 2 are

$$LP_{=}\sqrt{(x+l_x)^2+y^2+d^2}\tag{1}$$

$$RP_{=}\sqrt{(x-l_x)^2+y^2+d^2}\tag{2}$$

The phase φ between the two beams at point P can be calculated by

$$\varphi = \varphi_o - \varphi_r = \frac{(LP-RP)}{\lambda}\cdot 2\pi - 2k\pi\tag{3}$$

where λ is the wave length of the laser and k is an integer making φ vary from 0 to 2π.

After the rigid-body motion, the global displacements (d_x, d_y, d_z) of point P may be calculated by

$$d_x = S_x + R_z \cdot y\tag{4}$$

$$d_y = S_y + R_z \cdot x\tag{5}$$

$$d_z = S_z + R_x \cdot y + R_y \cdot x\tag{6}$$

where S_x, S_y and S_z are the translational displacements along x-axis, y-axis and z-axis respectively; R_x, R_y and R_z are the rotational displacements about the x-axis, y-axis and z-axis respectively.

Correspondingly, the paths of the observation beam and reference beam after the rigid-body motion are

$$LP' = \sqrt{(x+l_x+d_x)^2+(y+d_y)^2+(d+d_z)^2}\tag{7}$$

$$RP' = \sqrt{(x-l_x+d_x)^2+(y+d_y)^2+(d+d_z)^2}\tag{8}$$

The phase φ' between the two beams at point P' can be calculated by

$$\varphi' = \varphi'_o - \varphi'_r = \frac{(LP'-RP')}{\lambda}\cdot 2\pi - 2k'\pi\tag{9}$$

where k' is an integer making φ' to vary from 0 to 2π.

The phase change before and after the rigid-body motion is

$$\Delta = \varphi' - \varphi = \frac{[(LP'-RP')-(LP-RP)]}{\lambda}\cdot 2\pi - (k'-k)\cdot 2\pi$$
$$= \frac{[(LP'-RP')-(LP-RP)]}{\lambda}\cdot 2\pi - m\cdot 2\pi\tag{10}$$

where m is an integer.

In ESPI measurement, the in-plane displacement u in x-direction can be calculated by

$$u = \frac{\Delta \cdot \lambda}{4\pi \sin a} \tag{11}$$

where α is the incidence angle.

Putting Δ in Eqn. (10) into Eqn. (11), the displacement of point P after the rigid-body motion can be calculated:

$$u(P) = ((LP' - RP') - (LP - RP) - m)/(2\sin\alpha) \tag{12}$$

In the same way, it is possible to calculate the displacement of point O adjacent to P

$$u(O) = ((LO' - RO') - (LO - RO) - n)/(2\sin\alpha) \tag{13}$$

When rigid-body motion is small and the distance d between point P and O is short, the integer n is approximately equal to m. Therefore, the false strain between point P and O can be obtained from Eqn. (14).

$$\varepsilon = \frac{u(P) - u(O)}{d} \tag{14}$$

Assuming the translational and rotational rigid body displacements are 0.01mm and 0.02 ˚ respectively, the false strain fields in x-direction were determined using Eqn.(14). The distributions of false strains caused by the six individual rigid-body modes are illustrated in Fig. 3:

It can be found from Fig. 3 that the key factor causing the false strains around the center of the measuring surface is S_z. Based on the calculated false strain, corrections were made to eliminate the errors.

In the four-point bending test, both ESPI and strain gauges were used to measure the deformations in the pure bending zone at the middle span of the beam. LVDTs were installed to measure the rigid-body movements of the measuring surface. The false strains were estimated as the difference between ESPI results and strain gauge readings and a correction process was used to eliminate the false strains. A Comparison of strain gauge readings and ESPI results obtained before and after the correction process is shown in Fig. 4.

According to the false strains known and Eqn.1-14, theoretical translational movement S_z was calculated by inverse method and compared with the measured values in Fig. 5.

From the figure, very good agreement between the theoretical and measured rigid-body movement is observed, which demonstrates the validity of the proposed correction procedure.
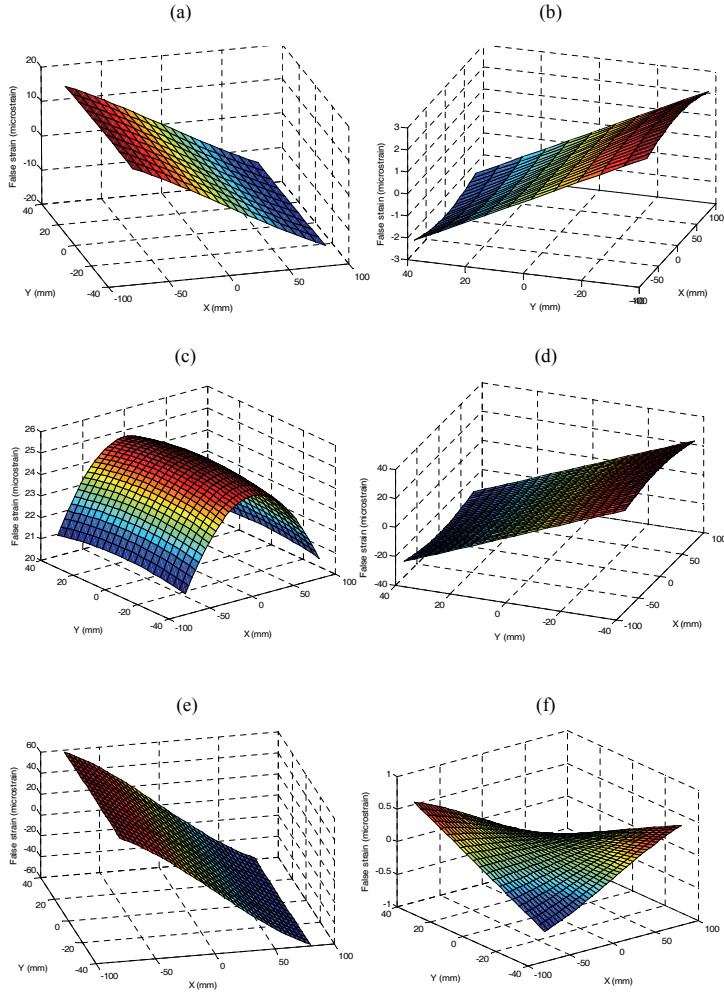
Figure 3: False strains due to different rigid-body modes: (a) S_x=0.01mm; (b) S_y=0.01mm; (c) S_z=0.01mm; (d) R_x=0.02 ˚; (e) R_y=0.02 ˚; (f) R_z=0.02 ˚

Detection of Crack Evolution by ESPI

Crack evolution was recorded by ESPI sensor in the three-point bending test on a notched beam. With a precast notch, the main crack initiated from the notch tip and propagated toward the loading point. In the ESPI measurement, crack can be defined as the discontinuity of the displacement contour, as shown in Fig. 6.

Due to the existence of coarse aggregates, the crack path cannot always keep on a straight line and may change in direction in order to round the aggregate, presenting sinuosity in its trajectory. After overlapping the displacement contour on the final fracture path, it is of benefit to observe and analyze the evolution of the
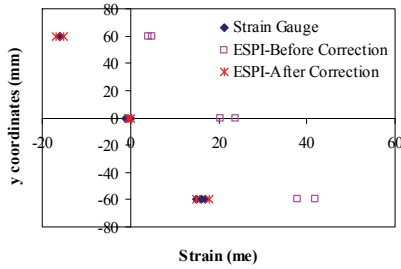
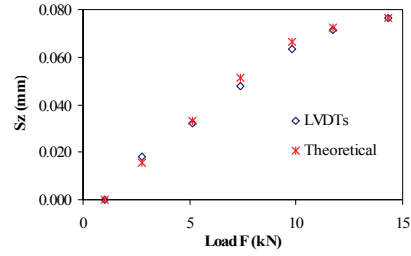Figure 4: Comparisons of ESPI results and strain gauge readings

Figure 5: Theoretical and measured displacement S_z
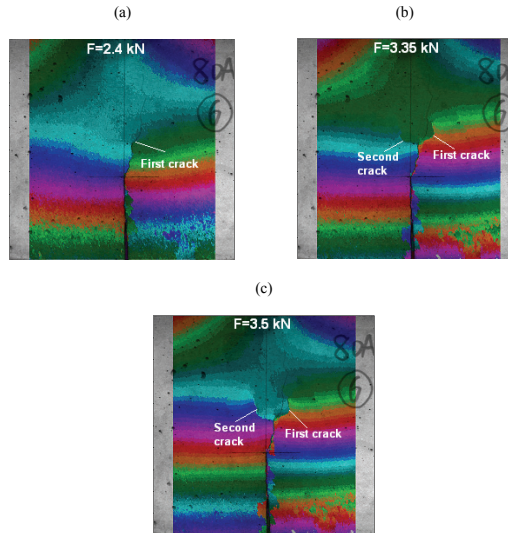
crack as shown in Fig. 6.

Figure 6: Displacement contour overlapped on the fracture path at different loading levels: (a) F=2.4 kN; (b) F=3.35 kN; (c) F=3.5 kN

As the load increased gradually, the concrete showed stable crack growth: (1) when load F=2.4 kN, the first crack occurred and propagated exactly along a single fracture path; (2) as the load F increased to 3.35 kN, the first crack propagated further until it met some obstacles. In order to consume the excessive energy, the crack was bifurcated into two branches, thus the second crack occurred and propagated; (3) as the load increased to 3.5 kN, both the first and second crack propagated further. After that, the first crack propagated quickly while the second crack closed, causing a sudden drop of the applied load and fracture failure of the beam.

The crack evolution implies that some cracks (e.g. the second crack) close during unloading. The present limited results revealed that the maximum crack

width along the second crack is about 2 μm while the crack width along the first crack is larger. It could be inferred that the crack width for a closed crack should be lower than 2 μm, otherwise it is probably an open crack and would propagate further when the load increases. Furthermore, when the relative displacement between two adjacent points is smaller than 0.09 μm, the concrete seems to be intact. If the relative displacement reaches 0.11 μm, discontinuity can be observed and cracks are expected to initiate. The minimum crack width for the occurrence of a microcrack is about 0.1 μm. The two critical crack widths coincide well with the experimental results proposed by Jia and Shah (1995). In their study, they found that the maximum crack width of fine cracks was less than 2 μm. In addition, when the first crack was detected, the crack opening displacement was about 0.249 μm, which is in the same order of magnitude of the present result (0.1 μm).

At different load levels, crack opening along the main crack trajectory is illustrated in Fig. 7. It can be observed from the figure that the crack tip is very sharp.
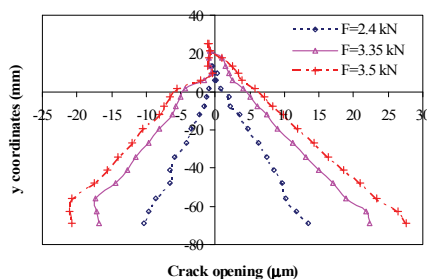

Figure 7: Crack opening along the crack trajectory

Finite Element Simulation Based on ATENA Software

ATENA software was used to simulate the global response of notched concrete beams. This software provides various material models to simulate different materials. SBeta Material is used in this study to model the material property of concrete. This material model takes into account all the aspects of real material properties of concrete in tension and compression. Several types of tension softening laws are available, for instant exponential softening curve, linear softening curve and SFRC softening curve. With these different tension softening laws, comparisons of load-deflection curves obtained from laboratorial test and ATENA simulation are illustrated in Fig. 8.

The comparisons imply that exponential softening law is more appropriate than other softening rules and good agreement is observed between the experimental and numerical results.
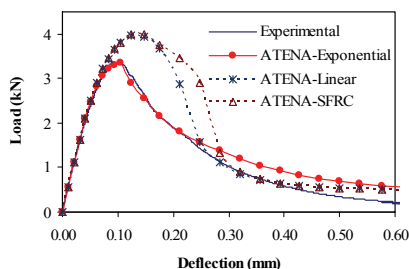
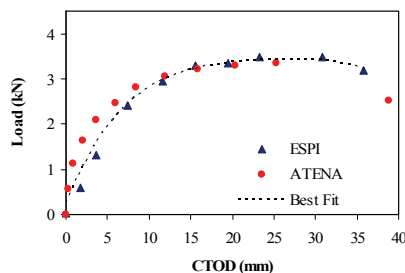Figure 8: Comparison of experimental and numerical load-deflection curves

Figure 9: Comparisons of experimental and numerical Load-CTOD curves

Using the exponential tensile softening rule, the crack tip opening displacement was computed. Fig. 9 compares the numerical values with that from ESPI. A very good agreement is observed. The results further revealed that when the beam failed at load=3.5 kN, the critical crack tip opening displacement is around 30-35 μm.

Conclusions

Through these experimental and numerical studies, the following summary can be arisen.

1. Based on the theory of geometrical optics, a correction procedure is proposed for eliminating the influence of rigid-body motion on the ESPI measurement. The correction procedure has been satisfactorily implemented. By comparing the theoretical rigid-body movements with the measured values by LVDTs, the validity of the procedure based on geometrical optics is demonstrated.

2. In the three-point bending test on the notched beam, a crack evolution process was observed by the ESPI sensor. After analyzing the evolution process, two critical crack widths were found: the minimum crack width of a microcrack is about 0.1μm and the minimum crack width for an open crack is about 2 μm. Further experimental studies would be carried out to confirm the values.

3. ATENA software was used to simulate the global response of concrete beam. The computed load-deflection curve using exponential tensile softening rule had a good agreement with the experimental result, which implies exponential softening law is more appropriate for concrete cracks. From both numerical and experimental results, the critical crack tip opening displacement is found to be around 30-35 μm.

Acknowledgement

References

1. **Celdolin, L.; Poli, S.D.; Iori, I.** (1987): Tensile Behavior of Concrete. *Journal of Engineering Mechanics,* vol. 113, no. 3, pp. 431-449.

2. **Castero-Montero, A.; Shah, S.P.; Miller, R.A.** (1990): Strain Field Measurement in Fracture Process Zone. *Journal of Engineering Mechanics,* vol. 116, no. 11, pp. 2463-2484.

3. **Jia, Z.; Shah, S.P.** (1995): Crack Detection in Concrete Using Real-time ESPI Technology. *Nondestructive Evaluation of Aging Aircraft, Airports, Aerospace Hardware, and Materials*, Proc. SPIE, vol. 2455, pp. 385-391.

4. **Haggerty, M.; Qing, L.; Labuz, J.F.** (2009): Observing Deformation and Fracture of Rock with Speckle Patterns. *Rock Mechanics and Rock Engineering*, Springer Wien.

5. **Cao, S.Y.; Chen, J.F.; Pan, J.W; Sun, N.** (2007): ESPI Measurement of Bond-Slip Relationships of FRP-Concrete Interface. *Journal of Composites for Construction*, vol. 11, no. 2, pp.149-160.

6. **Restivo, G.; Cloud, G.L.** (2008): Embedded Digital Speckle Pattern Interferometry for Three-dimensional Strain Analysis. *Experimental Mechanics*, vol. 48, no. 6, pp. 731-740.

7. **ATENA** (2000): ATENA program Document, Part 1 – Theory, Cervenka Consulting. Prague, Czech Republic.

8. **RILEM** (1990): TC89-FMT Fracture Mechanics of Concrete Test Methods - Determination of Fracture Parameters (K_{Ic}^s and CTOD$_c$) of Plain Concrete Using Three-point Bend Tests. *Materials and Structures*, vol. 23, no. 6, pp. 457-460.